GEOLOGY | THE GEOLOGICAL SOCIETY OF AMERICA®

https://doi.org/10.1130/G45880.1

Manuscript received 1 December 2018
Revised manuscript received 21 February 2019
Manuscript accepted 22 February 2019

Published online 22 March 2019

Ice-cliff failure via retrogressive slumping

Byron R. Parizek[1,2]*, Knut Christianson[3], Richard B. Alley[2], Denis Voytenko[4], Irena Vaňková[4], Timothy H. Dixon[5], Ryan T. Walker[6,7], and David M. Holland[4]

[1]Mathematics and Geoscience, The Pennsylvania State University, DuBois, Pennsylvania 15801, USA
[2]Department of Geosciences, and Earth and Environmental Systems Institute, The Pennsylvania State University, University Park, Pennsylvania 16802, USA
[3]Department of Earth and Space Sciences, University of Washington, Seattle, Washington 98195, USA
[4]Courant Institute of Mathematical Sciences, New York University, New York, New York 10012, USA
[5]School of Geosciences, University of South Florida, Tampa, Florida 33620, USA
[6]Earth System Science Interdisciplinary Center, University of Maryland, College Park, Maryland 20742, USA
[7]Cryospheric Sciences Laboratory, NASA Goddard Space Flight Center, Greenbelt, Maryland 20771, USA

ABSTRACT

Retrogressive slumping could accelerate sea-level rise if ice-sheet retreat generates ice cliffs much taller than observed today. The tallest ice cliffs, which extend roughly 100 m above sea level, calve only after ice-flow processes thin the ice to near flotation. Above some ice-cliff height limit, the stress state in ice will satisfy the material-failure criterion, resulting in faster brittle failure. New terrestrial radar data from Helheim Glacier, Greenland, suggest that taller subaerial cliffs are prone to failure by slumping, unloading submarine ice to allow buoyancy-driven full-thickness calving. Full-Stokes diagnostic modeling shows that the threshold cliff height for slumping is likely slightly above 100 m in many cases, and roughly twice that (145–285 m) in mechanically competent ice under well-drained or low-melt conditions.

INTRODUCTION

Ocean-ending ice in almost all cases forms a near-vertical cliff (Hollin, 1962) from which icebergs break (e.g., James et al., 2014; Murray et al., 2015). Faster submarine mass loss produces an overhang that breaks off to restore the cliff; faster subaerial mass loss creates analogous buoyant submerged ice that breaks and "falls" upward (Wagner et al., 2016). Observations show that sufficient warming removes floating ice shelves (Alley et al., 2015), leaving grounded ice cliffs from which icebergs break off directly. Recent modeling (DeConto and Pollard, 2016) and data (Wise et al., 2017) indicate that this could greatly accelerate ice-sheet mass loss, particularly within wide embayments in which outlet glaciers flow over retrograde beds.

The tallest modern subaerial ice cliffs are ~100 m (Scambos et al., 2011; Nick et al., 2013), occurring where ice shelves have been lost recently. Observations of these (e.g., Joughin et al., 2012) indicate that a large calving event generally shifts the cliff into ice too thick to float, although the cliff remains too short for rapid spontaneous failure. The loss of buttressing from the calved block is compensated by resistive stresses englacially and/or by increased side or basal drag upglacier. This increases deviatoric stresses and strain rates in and near the grounding zone (transitional region between grounded and floating ice), causing flow thinning until the ice approaches flotation. This likely allows greater tidal bending or other stresses and reduces basal friction, leading to another calving event (Joughin et al., 2012).

Taller cliffs have greater stress imbalance. Above some cliff-height threshold, which may slightly exceed 100 m (Hanson and Hooke, 2003; Bassis and Walker, 2012), the internal deviatoric stresses would exceed the ice strength, causing rapid failure without thinning to flotation. The pressure in a glacier from the weight of ice above exceeds that in adjacent air and water, with the largest imbalance immediately above the water line (Fig. 1A; Fig. DR3A in the GSA Data Repository[1]). Tension in the ice opposes the resulting horizontal differential pressure and tends to open near-vertical surface crevasses, as well as generates vertical deviatoric compression. The combined stresses promote failure along a surface slanting down to near the water line, favoring slumping (Fig. 1B; Figs. DR3B and DR3C) entirely analogous to slumping of rock cliffs and hillslopes. Removal of the weight of the slump mass produces an excess upward buoyancy force and an offsetting distribution of enhanced englacial deviatoric stresses, promoting basal crevassing and submarine block-rotation calving (Fig. 1B; Figs. DR3D–DR3F) (e.g., Murray et al., 2015), as documented for Jakobshavn Isbræ, Greenland (Walter et al., 2012; Sergeant et al., 2016).

Because the tallest modern ice cliffs are shorter than the estimated threshold height for rapid failure, we do not now expect frequent, spontaneous slumping followed by submarine calving. However, because the tallest cliffs approach the threshold height, we hypothesize that slumping followed by submarine calving would sometimes be observed, likely aided by tidal flexure or other processes. To test this hypothesis, we examined Greenland data, finding that, at times, slumping occurs near the onset of full-thickness calving. We also coupled new modeling with fracture-mechanics calculations to refine estimates of limiting cliff heights.

OBSERVATIONS

From 9 to 15 August 2014, we imaged the elevation and line-of-sight (LOS) velocity of Helheim Glacier, East Greenland (Fig. 2), with a real-aperture terrestrial radar interferometer (e.g., Voytenko et al., 2015) (Fig. DR2; see methods in the Data Repository). Here we focus on one major calving event (06:00–07:00 UTC, 12 August 2014; Figs. 1 and 3).

Beginning ~2 h before the event, acceleration along flow began for the ice behind the highest, northern ~1.5 km of the ~6-km-wide calving cliff, extending ~400 m upglacier to a series of prominent, recently expanding

*E-mail: parizek@psu.edu

[1]GSA Data Repository item 2019170, methods, supplementary figures, and supplementary movies, is available online at http://www.geosociety.org/datarepository/2019/, or on request from editing@geosociety.org.

CITATION: Parizek, B.R., et al., 2019, Ice-cliff failure via retrogressive slumping: Geology, v. 47, p. 449–452, https://doi.org/10.1130/G45880.1

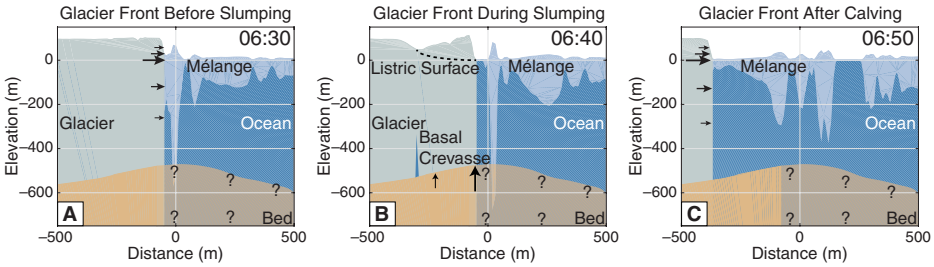

Figure 1. Helheim Glacier (East Greenland) ice-cliff geometry schematic during calving event. Glacier-front geometries along the last 1 km of the A-A′ profile shown in Figure 3A are from terrestrial radar interferometer data and assumed hydrostatic equilibrium for ice mélange before slumping begins (A), during slump (B), and after calving event concludes (C). Black arrows indicate relative glaciostatic and hydrostatic stress imbalance along ice front assuming negligible backpressure from mélange (A,C) and after mass loss due to slumping (B). Bed elevation is based on mass-conservation gridding (Morlighem et al., 2014) where available, and is unknown elsewhere, as denoted by question marks. Time (UTC, 12 August 2014) for each panel is noted in upper right corner.

crevasses. Acceleration likely continued until failure, with loss of interferometric coherency beginning ~10 min before calving, likely due to motion becoming too rapid to be captured by the sampling interval. Total anomalous forward motion of this block relative to the rest of the glacier prior to loss of coherency was <0.5 m. This northern mass was rotating top-upglacier (Figs. 3A and 3C) just before full-thickness calving (Figs. 1B, 3A, and 3C), consistent with a classic slump along a listric (concave upward) surface.

The initial slump was followed immediately by a large, full-thickness calving event across all except the southern ~1.5 km of the calving front (Fig. 3A), with the top rotating upglacier and temporarily reversing glacier motion (Figs. 3B and 3C). The post-calving subaerial glacier-front height stabilized at ~90 m (Figs. 1C and 3C). A similar Helheim slumping event, followed almost immediately by full-thickness calving, was filmed on 12 July 2010 (James et al., 2014).

Our data are in agreement with earlier GPS measurements of block rotation reversing glacier motion during calving (Murray et al., 2015). We also find a staged failure progressing along the ice front, starting with slumping of ice above and near the water line. Prior to our slumping event, the calving front was near or possibly at flotation, with unloading by slumping of the highest part of the calving front rapidly producing a large buoyancy-force imbalance (Fig. 1B; Fig. DR3D), allowing buoyancy-driven block rotation without ice-front advancement into deeper water.

Similar slump failures of a subaerial cliff (~100 m high) have been observed at Jakobshavn Isbræ, followed by large calving events that removed the ice beneath. Time matching of seismic recordings and video footage of one such event showed that a smaller-amplitude precursor signal matches the timing of the slumping event, followed by a characteristic, larger-amplitude, block rotation–sourced signal (Walter et al., 2012). Furthermore, in 38 of the 76 glacial earthquake events that were analyzed across Jakobshavn Isbræ, Helheim Glacier, and Kangerdlugssuaq Glacier in Greenland, similar precursory seismic signals were found, occurring 2–12 min before the main calving and/or block-rotation event (Olsen and Nettles, 2017). Other sources of precursory events are possible, including basal-crevasse propagation prior to block rotation triggering the slumping, but the coincident timing of listric failures with their precursory seismic signals is consistent with our hypothesis that slumping triggers block rotation.

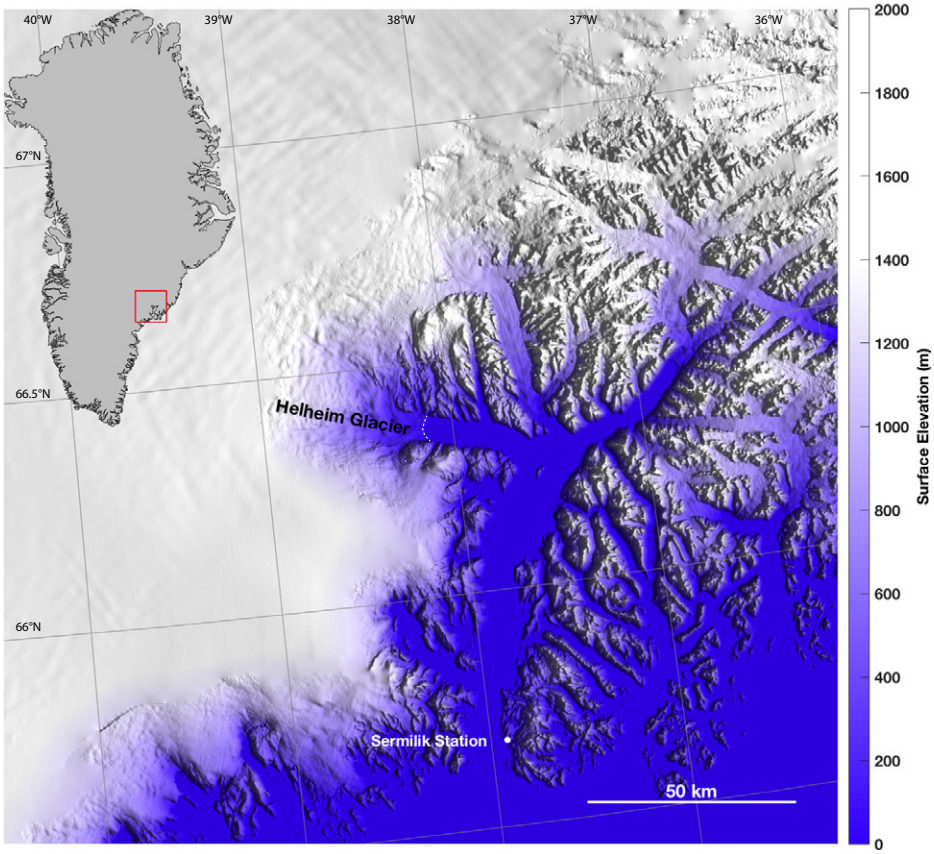

Figure 2. Location map of Helheim Glacier, East Greenland. Surface elevation (m) is from IceBridge BedMachine Greenland (https://nsidc.org/data/IDBMG4; Morlighem et al., 2017) and plotted using Arctic Mapping Tools (Greene et al., 2017). Ice-front position is approximated by dashed white curve.

PROCESS MODELING

We use (1) a diagnostic plane-strain Stokes model of idealized outlet glacier flow and (2) engineering and glaciological failure criteria (e.g., Schulson, 2001; see methods in the Data Repository) to mechanistically assess ice-cliff failure. Through large-ensemble numerical experiments, we evaluate tensile, shear, and compressive failure for a range of subaerial cliff heights as well as material and boundary parameters.

The ice-front pressure difference generates tensile ice stresses that tend to open nearly vertical surface crevasses behind the cliff. These may reach the bed if meltwater filled (Alley et al., 2005), but if well drained, extend downward a maximum of ~55%–60% of the subaerial cliff height in the limit of zero tensile ice strength (Fig. DR4A), at which point there is a transition to compression (Nye, 1957). (In crevasse fields such as those observed on Helheim's surface [Fig. DR2], penetration depths of air-filled crevasses are reduced somewhat [van der Veen, 1998] by stress interactions.)

Failure deeper than surface crevassing is most likely through compressive wing-crack growth (Renshaw and Schulson, 2001), which occurs

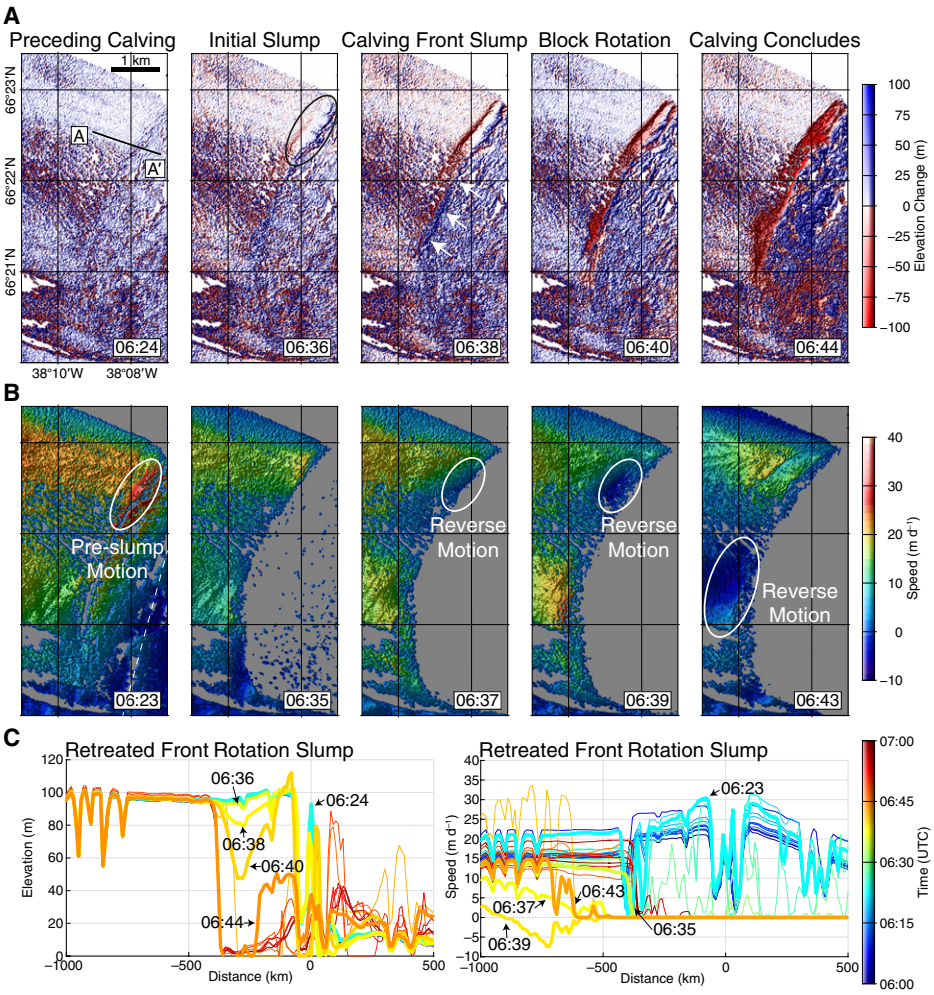

Figure 3. Helheim Glacier (East Greenland) elevation and speed during calving event. A: Surface elevation anomaly relative to 06:00 UTC, 12 August 2014. B: Line-of-sight speed during calving event, calculated as measured displacement between scenes (ranging from –1.39 cm to 5.56 cm, with 1.39 cm increment on existing color bar) divided by 120 s acquisition interval. Look direction of radar reference line is approximated by dashed white line. C: Surface elevation and speed profiles along profile A–A′ shown in first panel of A, colored by acquisition time with abscissa relative to initial calving front location. Thicker lines correspond to time slices depicted in A and B and are labeled with time stamp. In all panels, times (UTC, 12 August 2014) of data are noted.

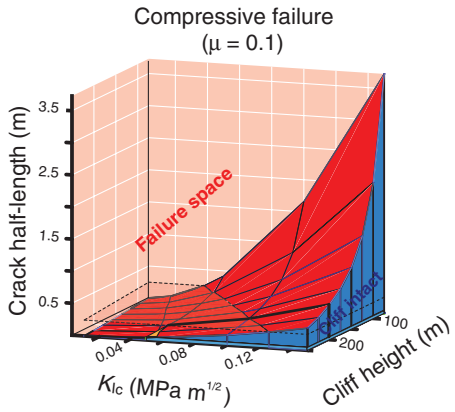

Figure 4. Parameter space for compressive failure. At and above red surface, compressive failure criteria have been met or exceeded for coefficient of static friction μ = 0.1. Blue slab at base of block represents typical crack half-length (c = 0.002–0.05 m) and fracture toughness (critical stress intensity factor K_{Ic} = 0.05–0.15 MPa m$^{1/2}$) ranges. Small orange corner in forefront represents failure within these parameter ranges. Horizontal plane with dashed black outline at c = 0.25 m intersects red failure surface along straight line, illustrating linear relationship between cliff height and fracture toughness at failure.

for lower stresses than shear failure (see methods in the Data Repository). Along-flow tension and coupled vertical compression behind an ice cliff cause shear slip along favorably oriented grain boundaries or other features (half-length *c*), which produces secondary wing cracks, if the greatest principal compressive strain rate exceeds the ductile-to-brittle transition (Fig. DR4C) so creep does not blunt the cracks and relieve the stress. Subsequent linkage of neighboring wing cracks creates a throughgoing damage zone angling down toward the cliff near the water line (Figs. DR4C and DR4D; Moore et al., 2010). For grain-face cracks of c = 5 cm (see methods in the Data Repository) and a low-end estimate of ice fracture toughness (critical stress intensity factor K_{Ic} = 0.05 MPa m$^{1/2}$; Moore et al., 2010), a connected failure zone forms from upper surface to cliff face for a minimum subaerial cliff height of ~200 m (145–285 m for doubling and halving *c*, respectively; Fig. 4). This height range agrees with a depth-integrated analytical estimate for failure of intact ice (Bassis and Walker, 2012).

This range provides an upper limit on stable cliff height, however, because (1) failure mechanisms can interact, reducing total strength; (2) we have not included subcritical crack growth, the resulting deformation, and subsequent stress loading of the remaining, still-competent ice; and (3) preexisting cracks much larger than individual grain boundaries typically exist at tall marine-terminating ice fronts that currently end in grounded or nearly grounded ice cliffs (Fig. DR2). Water pressure–driven fracturing from the surface also may lower the maximum stable cliff height.

DISCUSSION AND IMPLICATIONS

The Helheim Glacier and Jakobshavn Isbræ calving events highlighted here involved crevasse opening producing a near-vertical "head scarp", then block rotation likely on a listric surface extending downward and forward from the scarp base to the calving cliff just below the water line. Similar rotational slumps are widespread on hillslopes, and are suggested by previous modeling of subaerial ice cliffs (Hanson and Hooke, 2003; Bassis and Walker, 2012).

Near the water line, ice mélange can provide some cliff stability (e.g., Amundson et al., 2010) (see methods in the Data Repository), and the increase in water pressure with depth reduces the glaciostatic-hydrostatic stress imbalance across the calving front, so this imbalance is highest at the top of the mélange or at the water level in the absence of strong mélange. Any seawater seeping upglacier along cracks in the cliff face, or englacial drainage to a water table graded to the water line, would favor cliff instability by lubricating any failure surface and reducing the surface energy of new cracks (Griffith, 1921) and thus the work required for wing-crack formation. A failure surface running almost horizontally upglacier from just below the waterline could thereby connect through a failure surface from wing-crack interactions rising upglacier to the base of a tensile crevasse. Such a pattern matches our observations, and perhaps also those at Jakobshavn Isbræ (Walter et al., 2012), where nearly horizontal first seismic motion at the start of slumping may represent failure of the lower part of a listric surface and where precursor signals indicative of slumping occurred in >50% of the 43 recorded calving events between 2009 and 2013 (Olsen and Nettles, 2017).

Importantly, extensive and pervasive preexisting cracks near calving cliffs are much larger than the millimeter- to centimeter-scale grain size (to >10 m) (Fig. DR2), reducing

maximum stable cliff height (Fig. 4; see methods in the Data Repository). The 200-m-high ice front of Eqip Sermia in west Greenland is not vertical but slopes notably (~48°) (Engell, 2014; Lüthi and Vieli, 2016). Repeated subaerial slumping failure within its narrow fjord (~4 km) indicates that the ice is too weak to support 200 m cliffs. (Shallow calving-front water depth of only 20–40 m limits buoyant ice loss after slumping, preventing formation of a vertical cliff and thus providing stability against fast calving retreat.) The observed slumping of ~100 m cliffs, despite some stabilization from side drag and possibly from mélange, similarly suggests that the ice of Helheim Glacier and Jakobshavn Isbræ is much weaker than intact, undamaged ice, and/or we are still omitting key elements of the relevant mechanics.

Higher cliffs are more prone to failure. While stress increases linearly with cliff height, and creep inhibiting brittle failure increases approximately with the third power of the stress (see methods in the Data Repository), the rate of subcritical crack growth promoting failure increases approximately as the 30th power (e.g., Atkinson, 1984; Hallet, 1996) of the stress intensity. Therefore, higher cliffs have relatively less viscous relaxation due to the outpacing rate of crack growth.

Future cliff failure–driven rates of ice-sheet retreat and sea-level rise are likely to depend at least partially on the amount of surface melting, and on the rate at which damage occurs behind a cliff retreating into previously intact ice. Nevertheless, sufficiently high cliffs (~200 m) are likely to retreat by brittle failure, and thus to cause rapid sea-level rise at rates that surpass those predicted by parameterizations that limit wastage rates to those that have been recently observed.

ACKNOWLEDGMENTS

The work was supported by NASA grants NNX15AH84G (Parizek), NNX16AM01G (Christianson), NNX12AB69G (Christianson and Holland), NNX12AK29G (Dixon), and NNX12AD03A (Walker); U.S. National Science Foundation grants PLR-1443190 (Parizek), ANT-0424589 (Parizek and Alley), AGS-1338832 (Parizek and Alley), and PLR-1443284 (Walker); and New York University Abu Dhabi Research Institute grant G1204 (Holland). The field data-collection effort was organized by Denise Holland. We thank Kira Olsen for fruitful discussions, and both Kira Olsen and Meredith Nettles for freely sharing their scientific results. Finally, we would like to recognize the efforts of the Science Editor, Dennis Brown, and Ravindra Duddu and two anonymous reviewers, whose critical reviews were invaluable.

REFERENCES CITED

Alley, R.B., Dupont, T.K., Parizek, B.R., and Anandakrishnan, S., 2005, Access of surface meltwater to beds of subfreezing glaciers: Preliminary insights: Annals of Glaciology, v. 40, p. 8–14, https://doi.org/10.3189/172756405781813483.

Alley, R.B., Anandakrishnan, S., Christianson, K., Horgan, H.J., Muto, A., Parizek, B.R., Pollard, D., and Walker, R.T., 2015, Oceanic forcing of ice-sheet retreat: West Antarctica and more: Annual Review of Earth and Planetary Sciences, v. 43, p. 207–231, https://doi.org/10.1146/annurev-earth-060614-105344.

Amundson, J.M., Fahnestock, M., Truffer, M., Brown J., Lüthi, M.P. and Motyka, R.J., 2010, Ice mélange dynamics and implications for terminus stability, Jakobshavn Isbræ, Greenland: Journal of Geophysical Research, v. 115, F01005, https://doi.org/10.1029/2009JF001405.

Atkinson, B.K., 1984, Subcritical crack growth in geological materials: Journal of Geophysical Research, v. 89, p. 4077–4114, https://doi.org/10.1029/JB089iB06p04077.

Bassis, J.N., and Walker, C.C., 2012, Upper and lower limits on the stability of calving glaciers from the yield strength envelope of ice: Proceedings of the Royal Society of London A: Mathematical, Physical and Engineering Sciences, v. 468, p. 913–931, https://doi.org/10.1098/rspa.2011.0422.

DeConto, R.M., and Pollard, D.M., 2016, Contribution of Antarctica to past and future sea-level rise: Nature, v. 531, p. 591–597, https://doi.org/10.1038/nature17145.

Engell, N., 2014, Footage of Eqi Glacier July 2nd 2014: https://www.youtube.com/watch?v=Cxd-jA0_QIM (accessed October 2018).

Greene, C.A., Gwyther, D.E., and Blankenship, D.D., 2017, Antarctic Mapping Tools for Matlab: Computers & Geosciences, v. 104, p. 151–157, https://doi.org/10.1016/j.cageo.2016.08.003.

Griffith, A.A., 1921, The phenomena of rupture and flow in solids: Philosophical Transactions of the Royal Society of London, Series A: Containing Papers of a Mathematical or Physical Character, v. 221, p. 163–198, https://doi.org/10.1098/rsta.1921.0006.

Hallet, B., 1996, Glacial quarrying: A simple theoretical model: Annals of Glaciology, v. 22, p. 1–8, https://doi.org/10.1017/S0260305500015147.

Hanson, B., and Hooke, R.L., 2003, Buckling rate and overhang development at a calving face: Journal of Glaciology, v. 49, p. 577–586, https://doi.org/10.3189/172756503781830476.

Hollin, J.T., 1962, On the glacial history of Antarctica: Journal of Glaciology, v. 4, p. 173–195, https://doi.org/10.1017/S0022143000027386.

James, T.D., Murray, T., Selmes, N., Scharrer, K., and O'Leary, M., 2014, Buoyant flexure and basal crevassing in dynamic mass loss at Helheim Glacier: Nature Geoscience, v. 7, p. 593–596, https://doi.org/10.1038/ngeo2204.

Joughin, I., Smith, B.E., Howat, I.M., Floricioiu, D., Alley, R.B., Truffer, M., and Fahnestock, M., 2012, Seasonal to decadal scale variations in the surface velocity of Jakobshavn Isbræ, Greenland: Observation and model-based analysis: Journal of Geophysical Research, v. 117, F02030, https://doi.org/10.1029/2011JF002110.

Lüthi, M.P., and Vieli, A., 2016, Multi-method observation and analysis of a tsunami caused by glacier calving: The Cryosphere, v. 10, p. 995–1002, https://doi.org/10.5194/tc-10-995-2016.

Moore, P.L., Iverson, N.R., and Cohen, D., 2010, Conditions for thrust faulting in a glacier: Journal of Geophysical Research, v. 115, F02005, https://doi.org/10.1029/2009JF001307.

Morlighem, M., Rignot, E., Mouginot, J., Seroussi, H., and Larour, E., 2014, Deeply incised submarine glacial valleys beneath the Greenland ice sheet: Nature Geoscience, v. 7, p. 418–422, https://doi.org/10.1038/ngeo2167.

Morlighem, M., et al., 2017, IceBridge BedMachine Greenland, Version 3: Surface elevations: Boulder, Colorado, NASA National Snow and Ice Data Center Distributed Active Archive Center, https://doi.org/10.5067/2CIX82HUV88Y (accessed December 2018)

Murray, T., Selmes, N., James, T.D., Edwards, S., Martin, I., O'Farrell, T., Aspey, R., Rutt, I., Nettles, M., and Baugé, T., 2015, Dynamics of glacier calving at the ungrounded margin of Helheim Glacier, southeast Greenland: Journal of Geophysical Research: Earth Surface, v. 120, p. 964–982, https://doi.org/10.1002/2015JF003531.

Nick, F.M., Vieli, A., Andersen, M.L., Joughin, I., Payne, A., Edwards, T.L., Pattyn, F., and van de Wal, R.S.W., 2013, Future sea-level rise from Greenland's main outlet glaciers in a warming climate: Nature, v. 497, p. 235–238, https://doi.org/10.1038/nature12068.

Nye, J.F., 1957, The distribution of stress and velocity in glaciers and ice-sheets: Proceedings of the Royal Society of London, Series A: Mathematical and Physical Sciences, v. 239, p. 113–133, https://doi.org/10.1098/rspa.1957.0026.

Olsen, K., and Nettles, M., 2017, High-frequency seismic signals associated with glacial earthquakes in Greenland: Abstract C41D-1258 presented at American Geophysical Union Fall Meeting, New Orleans, Louisiana, 11–15 Dec.

Renshaw, C.E., and Schulson, E.M., 2001, Universal behavior in compressive failure of brittle materials: Nature, v. 412, p. 897–900, https://doi.org/10.1038/35091045.

Scambos, T.A., Berthier, E., and Shuman, C.A., 2011, The triggering of subglacial lake drainage during rapid glacier drawdown: Crane Glacier, Antarctic Peninsula: Annals of Glaciology, v. 52, p. 74–82, https://doi.org/10.3189/172756411799096204.

Schulson, E.M., 2001, Brittle failure of ice: Engineering Fracture Mechanics, v. 68, p. 1839–1887, https://doi.org/10.1016/S0013-7944(01)00037-6.

Sergeant, A., Mangeney, A., Stutzmann, E., Montagner, J.-P., Walter, F., Moretti, L., and Castelnau, O., 2016, Complex force history of a calving-generated glacial earthquake derived from broadband seismic inversion: Geophysical Research Letters, v. 43, p. 1055–1065, https://doi.org/10.1002/2015GL066785.

van der Veen, C.J., 1998, Fracture mechanics approach to penetration of surface crevasses on glaciers: Cold Regions Science and Technology, v. 27, p. 31–47, https://doi.org/10.1016/S0165-232X(97)00022-0.

Voytenko, D., Stern, A., Holland, D.M., Dixon, T.H., Christianson, K., and Walter, R.T., 2015, Tidally driven ice speed variation at Helheim Glacier, Greenland, observed with terrestrial radar interferometry: Journal of Glaciology, v. 61, p. 301–308, https://doi.org/10.3189/2015JoG14J173.

Wagner, T.J.W., James, T.D., Murray, T., and Vella, D., 2016, On the role of buoyant flexure in glacier calving: Geophysical Research Letters, v. 43, p. 232–240, https://doi.org/10.1002/2015GL067247.

Walter, F., Amundson, J.M., O'Neal, S., Truffer, M., Fahnestock, M., and Fricker, H.A., 2012, Analysis of low-frequency seismic signals generated during a multiple-iceberg calving event at Jakobshavn Isbræ, Greenland: Journal of Geophysical Research, v. 117, F01036, https://doi.org/10.1029/2011JF002132.

Wise, M.G., Dowdeswell, J.A., Jakobsson, M., and Larter, R.D., 2017, Evidence of marine ice-cliff instability in Pine Island Bay from iceberg-keel plough marks: Nature, v. 550, p. 506–510, https://doi.org/10.1038/nature24458.

Printed in USA